Enhanced Diagnostics Empowered by Improved Mechanical Vibration Component Extraction in Nonstationary Regimes

Fadi Karkafi[1,2], Jérôme Antoni[1], Quentin Leclère[1], Mahsa Yazdanianasr[3,4], Konstantinos Gryllias[3,4], and Mohammed El Badaoui[2,5]

[1] *INSA Lyon, LVA, UR677, 69621 Villeurbanne, France*

[2] *Safran Tech, Rue des Jeunes Bois – Châteaufort 78772 Magny–les–Hameaux, France*

[3] *KU Leuven, Department of Mechanical Engineering, Celestijnenlaan 300, 3001, Leuven, Belgium*

[4] *Flanders Make @ KU Leuven, Belgium*

[5] *UJM-St-Etienne, LASPI, UR3059, F-42023, Saint-Etienne, France*
fadi.karkafi@insa-lyon.fr
jerome.antoni@insa-lyon.fr
quentin.leclere@insa-lyon.fr
mahsa.yazdanianasr@kuleuven.be
konstantinos.gryllias@kuleuven.be
mohammed.el-badaoui@safrangroup.com

ABSTRACT

When analyzing vibration and sound signals from rotating machinery, accurately tracking individual orders is crucial for diagnostic and prognostic objectives. These orders correspond to sinusoidal components, also known as deterministic signals, whose amplitude and phase are modulated in response to the angular speed of the machine. The extraction of these components leads to a more comprehensive approach to differential diagnostics. When the machine operates under varying conditions, consistently tracking the orders becomes challenging, particularly in nonstationary regimes with very fast variations. Typically, this issue is addressed using common techniques such as Vold-Kalman filter (VKF), where the bandwidth of the selective filter is adjusted to handle the speed variations. However, in the presence of high-speed fluctuations, manual adjustment of these weights becomes difficult to balance the compromise between achieving accurate tracking by effectively filtering around the speed variations, and maintaining a low estimation bias by reducing noisy errors. To overcome this constraint, the proposed methodology is driven by the need to integrate speed fluctuations into an optimal solution using VKF. This adaptation involves the consideration of angular acceleration profiles within the innovation process. In this context, the bandwidths are automatically adjusted to their optimal values according to the machine's regime. Optimality is achieved by crafting a model dependent on the order signal-to-noise ratio (SNR) and the auto-regression coefficient. This optimization allows for a practical adjustment tailored to the distinctive characteristics of each order. A comprehensive analysis of the resulting model transfer function reveals crucial insights into the impact of the given order SNR and the speed fluctuations. Subsequently, the methodology undergoes performance assessment through simulations and synthetic cases, showcasing its viability and effectiveness across various regimes. Notably, its practical application is highlighted in envelope-based bearing diagnosis, during operations characterized by variable-speed conditions, thus underlining its promise in real-world applications.

1. INTRODUCTION

In mechanical systems, gears and rolling-element bearings play vital roles in power transmission, necessitating reliable operation (Randall & Antoni, 2011). Vibration and acoustic signals emitted by these mechanical pieces (Braun, 1986) exhibit distinct cyclostationary (CS) behavior (Antoni, 2009). Gears generate first-order cyclostationary (CS1) components with a periodic mean, forming a harmonic spectrum corre-

sponding to their fundamental period. Rolling-element bearings, on the other hand, exhibit second-order cyclostationary (CS2) components marked by periodic autocovariance and an instantaneous envelope. These distinctions are crucial for differential diagnosis (Antoni & Randall, 2002), providing insights into overall system health. In stationary conditions, Fourier analysis simplifies the identification of CS1 components, which are characterized by their corresponding amplitude and phase. This facilitated the rise of order tracking, enabling the extraction of these characteristic components. These orders correspond to sinusoidal signals, also termed deterministic components, wherein its amplitude and phase modulations are influenced by the machine angular speed with respect to a reference angle. Subtracting the tracked ones reveals residual random aspects, including the CS2 environment, offering a comprehensive diagnostic perspective.

However, as mechanical systems venture into varying nonstationary regimes, the complexity deepens. These distortions are mainly introduced by the change of the machine power intake and the effect of transmission from the excitation source to the sensor. Even with the application of angular resampling to address frequency modulations stemming from nonstationarity (McFadden, 1989; Bonnardot et al., 2005; Borghesani et al., 2012), the Fourier coefficients representing an order in the spectrum lose their pristine sparsity. This degradation arises from the dynamic evolution of the envelope and is highly emphasized in the presence of high speed fluctuations.

An essential technique in navigating this complexity is the Vold-Kalman filter (VKF) (Vold et al., 1997). Proposed by Vold and Leuridan, VKF has been a cornerstone in the estimation of individual order components instantaneous amplitude and phase. This selective filtering is adapted by adjusting its bandwidth correspondingly to handle nonstationary conditions for each order (M.-C. Pan & Wu, 2007b). Further advancements have led to schemes that simultaneously estimate multiple orders, such as the angular-displacement (AD) (M.-C. Pan & Wu, 2007a) and angular-velocity (AV) (M. Pan et al., 2016) VKF. Considering other notable methods, the Sliding Window Tracking (SWT) (Pai & Palazotto, 2009) technique was introduced to track the varying instantaneous amplitude of a noise-contaminated signal with a moving average. It employs a constant and a pair of windowed regular harmonics to fit the data, providing implicit noise filtering capabilities. Recently, the so-called local synchronous fitting (LSF) has been proposed (Abboud et al., 2022). It was introduced as an enhancement to the global one (GSF) (Daher et al., 2010) in the sense that it estimates a cyclic-nonstationary (CNS) mean, but through a local polynomial fit, using the well-known Savitsky-Golay filter (Savitzky & Golay, 1964). The properties of the filter was also discussed in (Abboud et al., 2019). Interested readers can refer to (Randall et al., 2011) for a comparison among more relevant separation techniques.

While SWT, LSF and VKF are highly accurate in terms of envelope estimation, their limitations become pronounced when mechanical systems transition into fast nonstationary variations. On the one hand, even though SWT attempts to address nonstationary behavior, it assumes a fixed sliding window length, which is not optimal for handling high speed fluctuations. On the other hand, LSF suffers from the estimation of the Fourier coefficient from the centered signal by applying a linear angle-invariant convolution. In fact, from a signal point of view, this operation aims at estimating the mean (trend) of a non-stationary time series. While the classical low-pass filtering is efficient when the noise is (angle-stationary), it can be highly compromised in the case of non-stationary noise, in particular when the noise is impulsive. Finally, while the VKF's bandwidth can be customized to handle nonstationary speed variations, the compromise between accurate tracking and maintaining low estimation bias is emphasized. In addition, within high speed variations, manually adapting the filter nonstationary parameters may pose challenges in achieving optimized solutions leading to unbalance this compromise. Other variants and extended versions of the filter considered tracking the components of interest by maximizing the kurtosis (Dion et al., 2013) and tuning the bandwidth accordingly (Feng et al., 2022) to take into account the high amplitude fluctuation. The high-speed environment necessitates a methodology that explicitly incorporates speed fluctuations into its definition. Consequently, rather than adjusting the filter bandwidth parameters to meet predefined objectives, an optimal approach involves integrating speed fluctuations directly into the model.

Therefore, the paper aims to present a novel VKF optimized solution where the innovation process is directly affected by the speed fluctuations, thus the bandwidth is automatically adapted, yielding stationary hyper-parameters to be tuned: the order signal-to-noise ratio (SNR) and the auto-regression coefficient. Section 2 states the problem with a particular attention to formulating the transmission path effect from a CNS view, followed by a detailed exposition of the methodology in Section 3. Sections 4 and 5 validate the effectiveness of the proposed solution on numerical and experimental signals. In light of the obtained results, the paper is sealed with a general conclusion in Section 6.

2. Problem Statement

This section introduces the basic model that will serve to define the solution, which consists of Fourier series whose complex exponentials are function of the variable angle, θ, being a reference angle in the machine, and the coefficients are only dependent on the speed $\omega = \frac{d\theta}{dt}$, with the load effect omitted. Practically, when vibration and acoustic responses are measured from rotating and reciprocating machinery, the effects of flow noise, turbulence, and transient events are captured, in addition to the sum of rotational dynamics $x(t)$, such that

the total measured signal $y(t)$ is:

$$y(t) = x(t) + \nu(t), \tag{1}$$

where $\nu(t)$ is causal and uncorrelated with $x(t)$ such that it doesn't affect its generation or behavior. A temporal representation of a rotating machine's excitation is defined as

$$x(t) = \sum_k a_k(t) e^{j2\pi\alpha_k\theta(t)+\Phi_k}, \tag{2}$$

where the harmonic cyclic order $\alpha_k = \frac{k}{\Theta}$ such that Θ stands for the angular period of the rotating component of reference, $\theta(t)$ is the angular position of the reference expressed in [rad] and a_k and Φ_k are respectively the slowly varying complex envelopes and phases. In the particular case of constant operating speed (i.e. $\theta(t) = \omega_0 t$), $a_k(t)$ become essentially constant over time, representing the Fourier coefficients in the harmonic series. In such scenario, the synchronous average (SA) is one of the most used tools to extract such components (Braun, 1975; McFadden, 1987), with minimum disruption in the residual signal (Randall et al., 2011). The SA simply consists in slicing the signal (often after an angular resampling step) into cycles equal to the rotation period of the mechanical piece of interest and performing an empirical average to reject (or reduce) non-synchronous components including noise and interfering components. However, in the case of speed varying excitation, the complex envelopes $a_k(t)$ become slowly varying and principally dependent on the operating speed and its fluctuations (Abboud et al., 2016). Despite mild conditions under which higher derivative orders can be neglected, high-speed fluctuations still induce non-stationary behavior in the envelope, potentially leading to inaccurate estimations for each given order. Therefore, the study focuses on the first derivative order to showcase the impact of speed fluctuations on the deterministic component evolution, given by:

$$x(t) = \sum_k a_k(\omega(t)) e^{j2\pi\alpha_k\theta(t)+\Phi_k}. \tag{3}$$

3. Proposed Methodology

The mechanical vibration nature specifies that the envelope functions should be smooth and slowly varying over time. One way of specifying this, is to demand that a repeated difference should be small, which satisfies the following VKF equation in stationary mode,

$$\frac{\partial^q a_k(t)}{\partial t^q} = \varepsilon_k(t), \tag{4}$$

where q is the derivative order and ε_k is a process of uncertainties that degrades the envelope. During this study and for simplicity, an order $q = 1$ will be elaborated. This leads to the fact that, in stationary regime, the envelope will tend to be constant with stationary uncertainties. However, this model turns out to be more sophisticated in the case where $\omega(t)$ is varying with respect to time because the uncertainties also become nonstationary. This can be formulated as follows:

$$\frac{\partial a_k(\omega)}{\partial \omega} = \varepsilon_k(\omega). \tag{5}$$

With the angular velocity varying over time, the application of the chain rule leads to the formulation:

$$\frac{\partial a_k(\omega(t))}{\partial t} = \dot{\omega}(t)\varepsilon_k(\omega(t)). \tag{6}$$

Given the existence of multiple regime scenarios, it is essential to consider both stationary and nonstationary modes, allowing for a generalized modeling approach. This results in envelope uncertainties attributed to

$$\frac{\partial a_k(\omega(t))}{\partial t} = (1 + \lambda\dot{\omega}(t))\varepsilon_k(\omega(t)), \tag{7}$$

where λ serves as a weighting coefficient. To optimize the model based on diverse domain processes derived from (1) and (7), a discrete-time realization is established. The main processes are expressed as follows:

$$\begin{cases} y_k[n] = a_k[n]e^{j\alpha_k\theta[n]} + \nu[n] \\ a_k[n] - \beta_k a_k[n-1] = (1 + \lambda\dot{\omega}[n])\varepsilon_k[n] \end{cases} \tag{8}$$

where $y_k[n]$ represents the raw noisy component corresponding to the k^{th} harmonic and β_k is the auto-regression coefficient whose value is close to 1. In the following, both $\nu[n]$ and $\varepsilon_k[n]$ are supposed to follow complex Gaussian normal distributions with respective variance σ_ν^2 and $\sigma_{\varepsilon_k}^2$: $\nu[n]$ ~ $CN(0, \sigma_\nu^2)$ and $\varepsilon_k[n]$ ~ $CN(0, \sigma_{\varepsilon_k}^2)$. Since $\dot{\omega}[n]$ and $\varepsilon_k[n]$ are independent, one can deduce that their product variance is equal to $(1+\lambda\dot{\omega}[n])^2 \times \sigma_{\varepsilon_k}^2$. Thus, the definition of the two processes:

$$P_1 : \mathbf{Y}_k - \mathbf{A}_k\mathbf{E}_k = \mathbf{V}, \tag{9}$$

where $\mathbf{Y}_k$, $\mathbf{E}_k$ and $\mathbf{V}$ are expressed as follows:

$$\mathbf{Y}_k = \begin{bmatrix} \vdots \\ y_k[n] \\ \vdots \end{bmatrix}, \mathbf{E}_k = \begin{bmatrix} \ddots & & \\ & e^{j\alpha_k\theta[n]} & \\ & & \ddots \end{bmatrix}, \mathbf{V} = \begin{bmatrix} \vdots \\ \nu[n] \\ \vdots \end{bmatrix}.$$

$$P_2 : \mathbf{D}_k\mathbf{A}_k = \mathbf{\Psi}\xi_k, \tag{10}$$

such that $\mathbf{A}_k$ and the sparse matrix $\mathbf{D}_k$ are expressed as

$$\mathbf{A}_k = \begin{bmatrix} \vdots \\ a_k[n] \\ \vdots \end{bmatrix}, \mathbf{D}_k = \begin{bmatrix} 1 & 0 & 0 & \dots & 0 \\ -\beta_k & 1 & 0 & 0 & 0 \\ 0 & -\beta_k & 1 & 0 & 0 \\ \vdots & 0 & \ddots & \ddots & 0 \\ 0 & 0 & 0 & -\beta_k & 1 \end{bmatrix},$$

along with $\mathbf{\Psi}$ and $\boldsymbol{\xi}_k$ expressed as:

$$\mathbf{\Psi} = \begin{bmatrix} \vdots \\ 1 + \lambda\dot{\omega}[n] \\ \vdots \end{bmatrix}, \boldsymbol{\xi}_k = \begin{bmatrix} \vdots \\ \varepsilon_k[n] \\ \vdots \end{bmatrix}.$$

3.1. A Posterior Estimate of the Envelope

With regards to the envelope's dependencies, one can explicitly describe its likelihood and prior distribution. As a result, the a posterior estimation of A_k can be defined by the Maximum a posteriori estimate (MAP):

$$\begin{aligned} \hat{\mathbf{A}}_k &= \text{Argmax}(P(\mathbf{A}_k|\mathbf{Y}_k)) \\ &\propto \text{Argmax}(P(\mathbf{Y}_k|\mathbf{A}_k)P(\mathbf{A}_k)). \end{aligned} \tag{11}$$

After setting $\mathbf{\Gamma}_k = \mathbf{D}_k\mathbf{A}_k$ to simplify the process formulation, the Bayes Theorem can be applied to P_2 in order to compute $P(\mathbf{A}_k)$ as follows:

$$P(\mathbf{A}_k) = \int P(\mathbf{A}_k, \mathbf{\Gamma}_k) d\mathbf{\Gamma}_k. \tag{12}$$

One can deduce from Eqs (10) and (12) that

$$P(\mathbf{A}_k) = P(\mathbf{\Gamma}_k)|\mathbf{D}_k|, \tag{13}$$

To initiate the MAP estimate, the likelihood conditional probability $P(\mathbf{Y}_k|\mathbf{A}_k)$ and the prior one $P(\mathbf{A}_k)$ can be expressed accordingly:

$$P(\mathbf{Y}_k|\mathbf{A}_k) = \frac{1}{\pi\sigma_\nu^{2N}} e^{-\frac{\|\mathbf{Y}_k - \mathbf{E}_k\mathbf{A}_k\|^2}{\sigma_\nu^2}}, \tag{14}$$

$$P(\mathbf{A}_k) = \frac{1}{\pi\sigma_{\varepsilon_k}^{2N}\mathbf{\Omega}} e^{-\frac{\|\mathbf{A}_k^T\mathbf{D}_k^T\mathbf{\Omega}^{-1}\mathbf{A}_k\mathbf{D}_k\|}{\sigma_{\varepsilon_k}^2}} |\mathbf{D}_k|, \tag{15}$$

where $[\mathbf{\Omega}]_{ij} = \delta_{ij}\mathbf{\Psi}[i]^2$ and δ_{ij} is the Kronecker delta. Plugging Eqs (14) and (15) into Eq (11) result minimizing an objective function $J(\mathbf{A}_k)$ represented by:

$$J(\mathbf{A}_k) \approx \frac{\|\mathbf{Y}_k - \mathbf{E}_k\mathbf{A}_k\|^2}{\sigma_\nu^2} + \mathbf{A}_k^T\mathbf{D}_k^T\frac{\mathbf{\Omega}^{-1}}{\sigma_{\varepsilon_k}^2}\mathbf{D}_k\mathbf{A}_k \tag{16}$$

such that $\mathbf{M}^T$ represents the transpose of $\mathbf{M}$. In order to find the minimum, the derivative of $J(\mathbf{A}_k)$ with respect to the variable of interest $\mathbf{A}_k$ is set to 0: $\frac{\partial J(\mathbf{A}_k)}{\partial \mathbf{A}_k} = 0$. As a result, the estimated $\hat{\mathbf{A}}_k$ can be computed as

$$\hat{\mathbf{A}}_k = \left(\mathbb{I} + \frac{\sigma_\nu^2}{\sigma_{\varepsilon_k}^2}\mathbf{D}_k^T\mathbf{\Omega}^{-1}\mathbf{D}_k\right)^{-1}\mathbf{E}_\mathbf{k}^\mathbf{H}\mathbf{Y}_k \tag{17}$$

such that $\mathbf{E}_k^H$ is the conjugate of $\mathbf{E}_k$ and $\mathbb{I}$ is the identity matrix. It can be identified from the resulted model that, $\hat{\mathbf{A}}_k$ depends on the constant ratio $\rho_k = \frac{\sigma_\nu^2}{\sigma_{\varepsilon_k}^2}$ which is none other than the inverse SNR of the k^{th} harmonic.

3.2. Filter Frequency Response Function

In order to interpret the model frequency response function (FRF), a simple scheme is considered in Fig. 1 such that the objective is to find $|H_k(f)|^2$ that would result in $A_k(f)$ from $Y_k(f)$. In order to define $|H_k(f)|^2$, the speed $\omega(t)$ is assumed

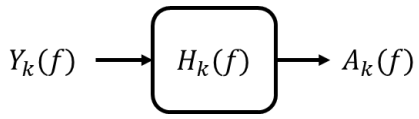

Figure 1. Scheme illustrating the transfer function $H_k(f)$ processing input $Y_k(f)$ to produce output $A_k(f)$.

to be constant or slowly varying, ensuring fixed frequency and allowing the FRF to make sense for each frequency, which results in $\dot{\omega}[n] \approx 0$. In addition, it is noteworthy that, as the filter automatically adapts to speed fluctuations, its stationary parameters remain valid regardless of the operating regime. Consequently, the FRF will be analyzed primarily under stationary conditions, ensuring correct parameters estimation. Recalling the processes described in Eq. (8), its respective power spectral densities would take the following form:

$$S_{Y_k}(f) = E|Y_k(f)|^2 = E|A_k(f)|^2 + E|V(f)|^2, \tag{18}$$

$$S_{A_k}(f) = E|A_k(f)|^2 = \frac{E|\xi_k(f)|^2}{|1 - \beta_k e^{-j2\pi f}|^2}. \tag{19}$$

Knowing that $E|V(f)|^2 = \sigma_\nu^2$ and $E|\xi(f)|^2 = \sigma_\varepsilon^2$, S_{H_k} can be computed as follows:

$$S_{H_k}(f) = \frac{S_{A_k}(f)}{S_{Y_k}(f)} = \frac{1}{1 + \rho_k|1 - \beta_k e^{-j2\pi f}|^2}. \tag{20}$$

Based on Eq. (20), it seems to behave like a low pass filter. For a comprehensive understanding, it is crucial to investigate the parameters of the FRF and the frequencies associated with typical filters. In this analysis, the following parameters are defined in the logarithmic:

$$\begin{cases} \ln(|H(0)|^2) = -\mu_0 \\ \ln(|H(f_p)|^2) = -\mu_p \\ \ln(|H(f_s)|^2) = -\mu_s \end{cases} \tag{21}$$

such that

1. f_p: The passband frequency.
2. f_s: The stopband frequency.
3. $-\mu_0$: Log of the FRF at $f = 0$.
4. $-\mu_p$: Log of the FRF at the passband frequency f_p.
5. $-\mu_s$: Log of the FRF at the stopband frequency f_s.

To illustrate these parameters, consider Figure 2 that depicts an example of lowpass filter with the passband frequency f_p, stopband frequency f_s and other associated parameters.

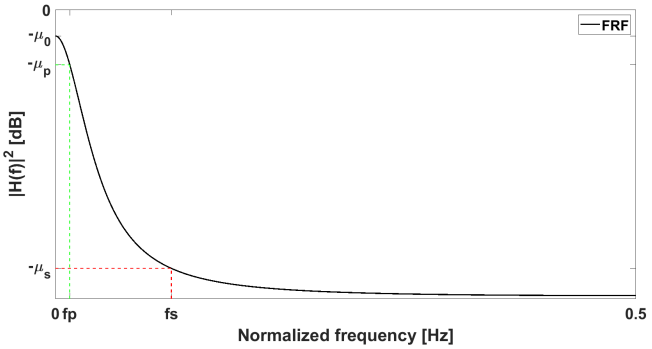

Figure 2. Illustration of a theoretical first-order lowpass filter with the corresponding characteristics.

In Figures 3a and 3b, the FRF for the proposed filter is illustrated under various conditions. Each figure depicts the FRF for different values of ρ_k, showcasing the impact of this parameter on the filter's behavior.

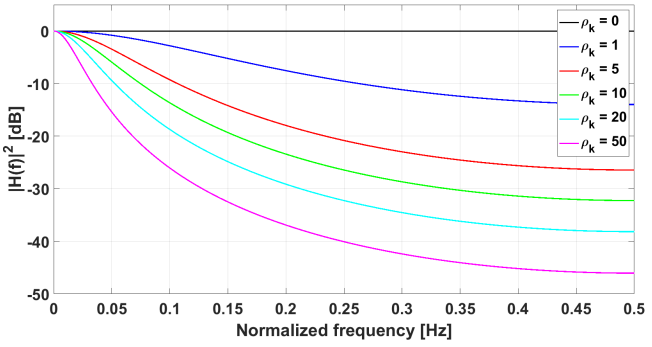

(a)

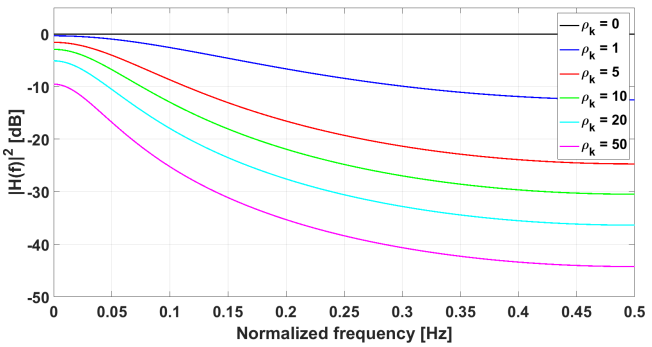

(b)

Figure 3. Plots of the frequency response function using various ρ_k values with respect to (a) $\beta_k = 1$ and (b) $\beta_k = 0.8$.

Furthermore, the illustrations explore the influence of β_k, presenting results with $\beta_k = 1$ & $\beta_k = 0.8$ respectively. The distinctive curves in each plot reveal the sensitivity of the filter to the model parameters ρ_k and β_k, providing valuable insights into its performance characteristics.

4. Numerical Experiment

Deterministic components encountered in rotating machine signals operating under nonstationary regimes are generally sinusoidal components whose amplitudes and phases are modulated through smooth functions. These amplitude modulations typically arise from resonance encounters or shifts in internal forces. Phase alterations may stem from variations in time delays resulting from mechanical system transfer functions interacting with excitation frequencies, or from torsional oscillations in shafts. To capture these dynamics, the following sinusoidal model is adopted:

$$y[n] = \sum_{k=1}^{3} a_k[n] sin\left(2\pi k \sum_{m=0}^{n} \omega[m] + \Phi_k[n]\right) + \nu[n] \tag{22}$$

where

1. $y[n]$ is the generated signal sampled at 10kHz over a 10 second acquisition window (i.e. resulting in 100 ksamples)
2. $\omega[n]$ stands for the instantaneous frequency of the reference rotating shaft (i.e. the fundamental frequency of the process associated with the order 1) simulated using a first order autoregressive process (see top Figure 4),
3. $a_k[n]$ and $\Phi_k[n]$ are respectively the amplitude and the phase modulations associated with the k^{th} harmonic (see middle and bottom Figure 4), made of linear combination of the square of $\omega[n]$, $\nu[n]$ is a stationary gaussian noise.

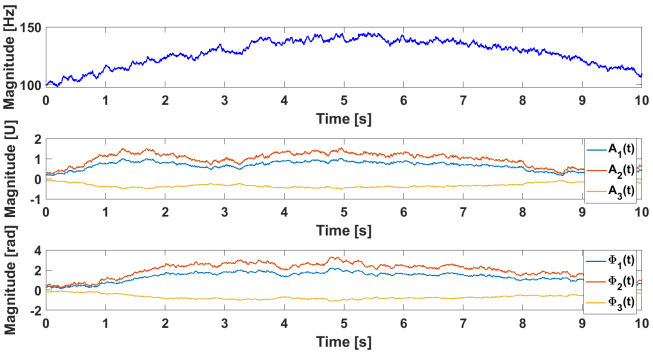

Figure 4. Plots of: (top) the speed constructed using a first order auto-regressive process, (middle) the 3 amplitudes $a_k[n]$ and (bottom) the 3 phase modulations $\Phi_k[n]$ associated with the sinusoids of the synthetic signal.

The signal-to-noise (power) ratio equals -10dB. The proposed methodology is implemented on the signal, alongside three other methods for comparative analysis: SWT, LSF, and VKF with stationary bandwidth in order to assess the efficacy of the speed adaptation proposed in this study. For SWT, the window length was optimized to achieve the best performance,

resulting in a length of 125 samples per sliding window. LSF is applied to the signal after resampling in the angular domain, employing a polynomial order of 5 and a window length of 75 samples. The conventional and proposed VKF parameters, namely β_k and ρ_k, are fine-tuned to achieve the values presented in Table 1. These parameters are crucial as they

Table 1. Filter tuned parameters for the simulation case.

Parameters	Value
β_k	$\{0.988, 0.991, 0.957\}$
ρ_k	$\{45, 35, 75\}$
λ	1

directly impact the filtering process and subsequent signal analysis. The actual (noise-free) signal, the estimated signals and corresponding errors are displayed in Figure 5 for each method. It is clear from the figure that the proposed estimation is more accurate than the other used techniques: Table 2 shows that the proposed error signal has a significantly lower relative mean error compared to SWT, LSF and VKF.

Table 2. Relative mean errors of each used method.

Used method	Relative mean error %
SWT	4.18
LSF	8.44
VKF	6.60
Proposed method	**1.84**

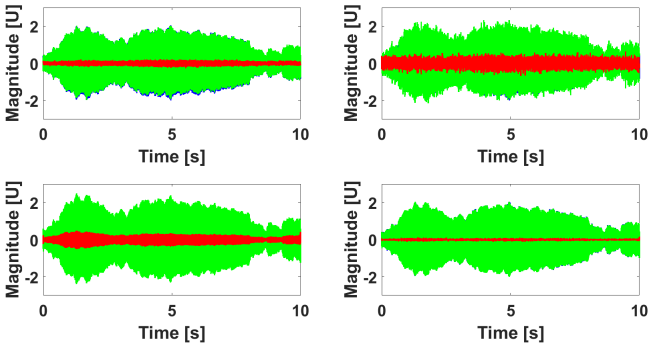

Figure 5. The actual noise-free signal (blue line), the deterministic signal estimate (green line) and the corresponding errors (red line) using the (top-left) SWT method, (top-right) LSF method, (bottom-left) conventional VKF and (bottom-right) proposed method.

For further interpretation of the proposed methodology, the envelope estimation is visualized in Figure 6 to assess the evaluation with respect to the reference one (actual envelope). It is essential to see how the model kept track of the envelope related to each of the 3 cyclic orders. In addition, the FRF along with the extracted component of the first cyclic order are displayed in Figures 7 and 8 to have a better comprehensive understanding of the model with respect to the chosen

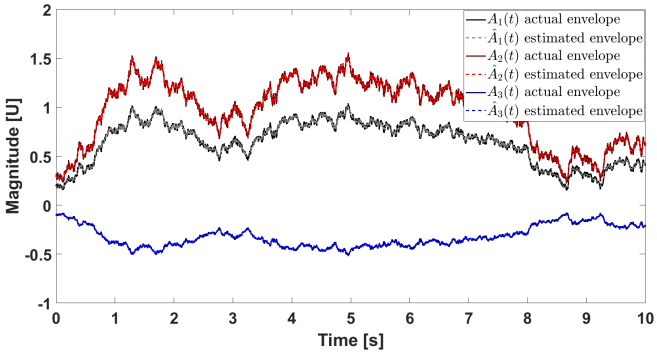

Figure 6. Plot showing the assessment of the estimated envelopes (dashed lines) with respect to the actual ones (full lines).

parameters β_k and ρ_1. It can be seen in the resiudal within the Figure 8 that the first tracked order was completely extracted after using the FRF displayed in 7. After iterating

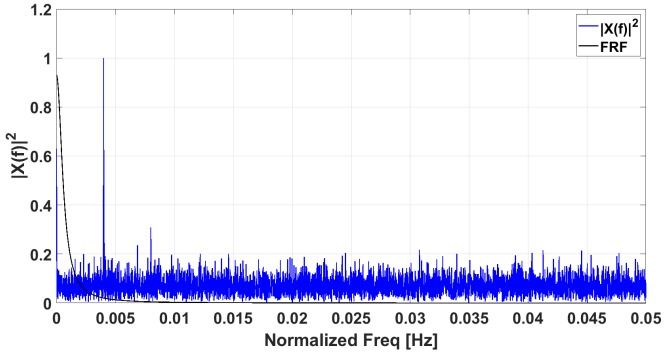

Figure 7. Scaled squared order spectrum of demodulated angular signal with FRF for first order, illustrating passed and rejected frequencies.

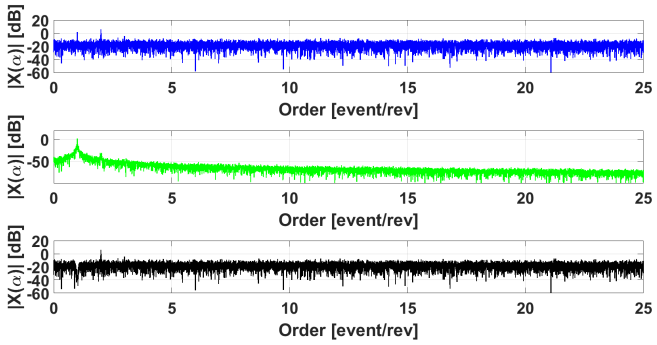

Figure 8. Order spectrums of: (top) the raw signal, (middle) the first extracted component and (bottom) the residual signal.

over the 3 orders, the spectrograms of the raw, extracted and residual signals are displayed in Figure 9. Since the signal is generated in a nonstationary regime, time-frequency representation (TFR) is a popular tool to present those time-variant components before resampling into the angular domain. This

is done to show that the proposed methodology filters well the 3 harmonics of interest from the raw signal.

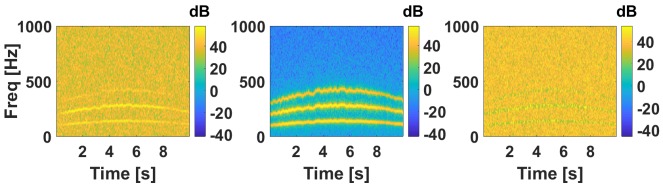

Figure 9. Simulation close-up spectrograms of the generated signals. (Left) Raw signal, (Middle) extracted components, and (Right) residual signal.

5. Application

This section presents the evaluation of the methodology using real experimental data acquired from the KU Leuven Diagnostic test rig (Yazdanianasr et al., 2024), as depicted in Figure 10. The test rig comprised an electric drive motor, a first housing containing a healthy bearing, and a second housing with two cases: one featuring large damage to the inner race of the test bearing and another case involving small damage to the outer race. The bearings used are SKF 2206 ETN9 bearings. The experimental setup also included the mounting of two ICP accelerometers (PCB-model number 352A10) on the housing of the bearings. Additionally, two B&k type 4188 microphones were installed as seen in the figure of the test rig. Furthermore, a smartphone, capturing through its microphone (considered as the low quality microphone in this acquisition), was placed behind the second microphone. Finally, an encoder was installed on the end of the electric motor to keep track of the angular position, providing a reliable estimate of the angular speed. Notably, the sampling frequency for all sensors, excluding the smartphone, was about 102.4 kHz. Given the smartphone's sampling frequency of 44.1 kHz, resampling was necessary to synchronize its data with that of the other sensors. The experiment aims to discern

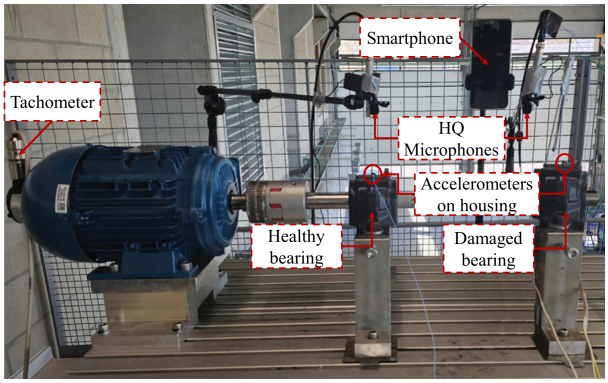

Figure 10. KU Leuven Diagnostic test rig.

both types of faults mentioned before, captured under a non-stationary regime. Naturally, signals from the accelerometer positioned on the upper part of the damaged bearing housing provide insights into significant damage to the inner race fault case. However, the experiment goes a step further by utilizing signals from the smartphone, which captures data from a distance near the upper part of the housing, revealing small damage for the outer race case. This small fault presents a significant challenge, as its detection amidst the presence of CS1 components can be particularly difficult to achieve, polluted by additional noise from the outside environment. Therefore, the experiment will be divided into two cases: the Large Inner Race Fault Case and the Small Outer Race Fault Case.

5.1. Large Inner Race Fault

In this initial experiment, the speed profile employed, as depicted in Figure 11, primarily exhibited random behavior to provide a highly nonstationary condition. The corresponding raw accelerometer signal is also displayed in Figure 12. In

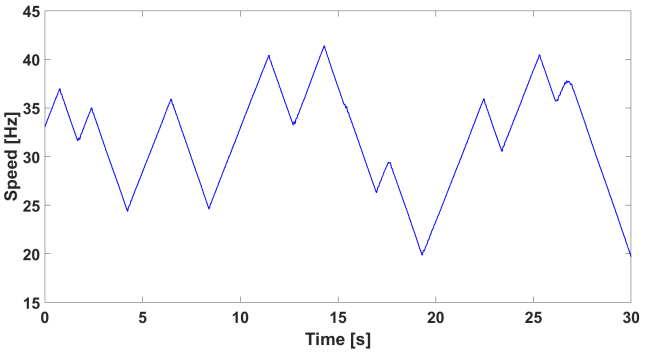

Figure 11. First experiment random walk-like speed profile

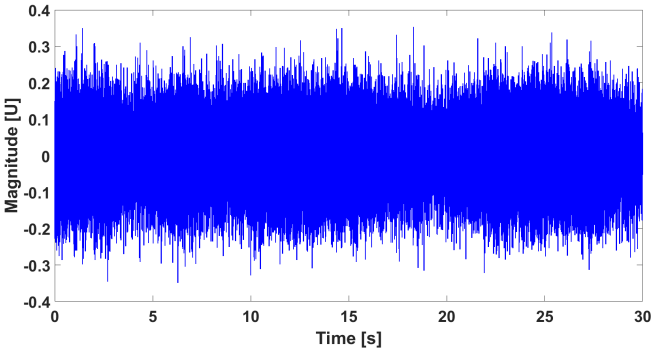

Figure 12. First experiment raw accelerometer signal depicting the varying signal envelope.

the initial phase, pinpointing the bandwidth containing critical CS2 information is essential. Utilizing the well known kurtogram (Antoni & Randall, 2007) can facilitate the detection of pertinent details. In this instance, the bandwidth yielding the highest kurtosis fell within the range of [815, 865] shaft order. Consequently, the CS1 orders to be tracked align with the speed components that reside within the frequency

band of [16300, 17300] Hz. After identifying 6 speed dependent orders, their deterministic components were extracted using the proposed technique. Upon fine-tuning the parameters of the methodology, the values shown in Table 3 were attained. The speed fluctuation weight λ was set the same for

Table 3. Filter tuned parameters for the first experiment.

Parameters	Value
β_k	$\{0.995, 0.987, 0.999, 0.979, 0.988, 0.954\}$
ρ_k	$\{4320, 7664, 4211, 8853, 5333, 9912\}$
λ	0.01

all harmonics to control the stationary-nonstationary adjustment. To evaluate the impact of the model with the specified parameters, close-up spectrograms of the raw signal, the extracted CS1 components, and the residual are presented in Figure 13. This enables observation of the significant attenuation of the speed components, tracked with the defined orders. Additionally, the speed profiles corresponding to the tracked orders are displayed with red dashed lines. The described processing steps are applied both to the raw signal and the residual one to compare the attenuation of speed dependent deterministic components. Initially, angular resampling is performed to mitigate frequency modulations. Subsequently, both angular signals undergo filtering within the specified bandwidth to isolate bearing signature information. A Hilbert transform is then employed to extract the envelope of the resulting complex signal. Finally, the squared envelope spectrum (SES) of the angular filtered signals is computed for evaluation. Figure 14 compares both SES, emphasizing the bearing fault contribution after the elimination of the extracted components. The analysis reveals that while extracting deterministic components, it also impacted the BPFI modulations. These modulations, typically associated with CS2 components, showed attenuation due to interactions with deterministic speed components. This suggests that the BPFI signature, not being entirely random, led to the attenuation of its deterministic part.

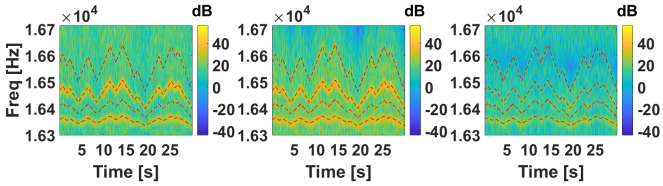

Figure 13. First experiment close-up spectrograms of the vibration signals. (Left) Raw signal, (Middle) extracted components, and (Right) residual signal with tracked speed profiles (red dashed lines).

5.2. Small Outer Race Fault

In the second experiment, the utilized speed profile, illustrated in Figure 15, primarily demonstrated a steady-hop behavior. The corresponding raw smartphone microphone signal is also displayed in Figure 16 to demonstrate the variation of its envelope in tandem with the changes in speed. Similar to the initial steps taken in the first experiment, efforts were made to identify the bandwidth containing crucial CS2

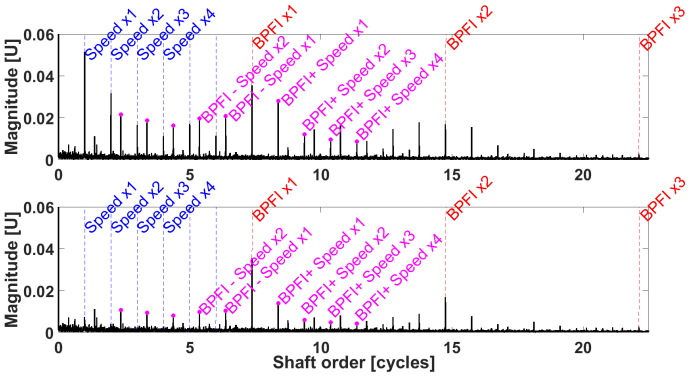

Figure 14. Squared envelope spectrum of: (top) raw signal and (bottom) residual signal highlighting the BPFI multiples (red dashed lines), the speed harmonics (blue dashed lines) and the modulations of the first BFPI (purple markers), showing the attenuation of the speed components in the residual one.

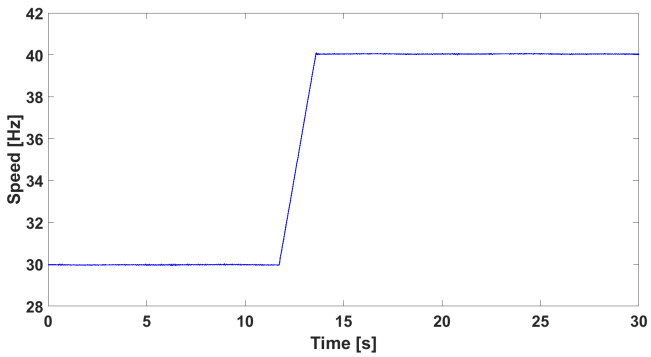

Figure 15. Second experiment steady-hop speed profile

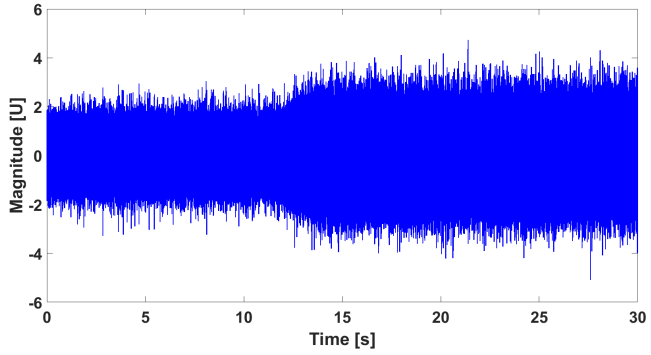

Figure 16. Second experiment raw smartphone microphone signal depicting the variation of the signal envelope mirroring the changes in the speed profile.

information. However, in this instance, the analysis was performed using data acquired from the smartphone instead of the accelerometer. The analysis revealed that the bandwidth with the highest kurtosis, as determined by the kurtogram, fell within the range of [333, 353] shaft order. For the second experiment, a similar process was followed to identify 8 speed dependent orders and extract their deterministic components using the proposed technique. The parameters of the methodology were fine-tuned to achieve the values described in Table 4. To assess the impact of the model with these specified parameters, close-up spectrograms of the raw signal, the extracted CS1 components, and the residual are provided in Figure 17 which facilitates observation of the significant attenuation of the speed components tracked with the defined orders.

Table 4. Filter tuned parameters for the second experiment.

Parameters	Value
β_k	$\{0.947, 0.955, 0.994, 0.936, 0.961, 0.887, 0.947, 0.984\}$
ρ_k	$\{12206, 11791, 8645, 13662 9197, 21111, 12206, 10167\}$
λ	0.01

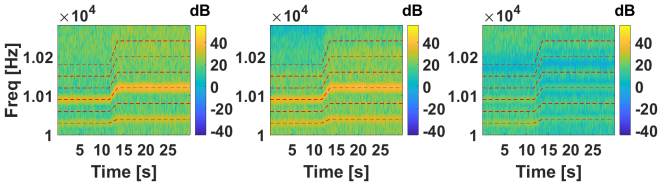

Figure 17. Second experiment close-up spectrograms of the vibration signals. (Left) Raw signal, (Middle) extracted components, and (Right) residual signal with tracked speed profiles (red dashed lines).

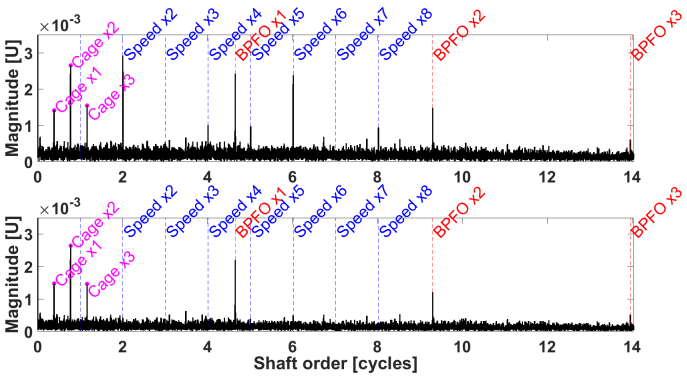

Figure 18. Squared envelope spectrum of: (top) raw signal and (bottom) residual signal highlighting the BPFO multiples (red dashed lines), the speed harmonics (blue dashed lines) and the cage frequencies (purple markers), showing the attenuation of the speed components in the residual one.

Similarly, for the second experiment, the processing until the computation of the SES was carried out on the raw signal and its residual to identify the Ball Pass Frequency Outer Race (BPFO). A comparison of both raw and residual SES are illustrated in Figure 18.

6. Conclusion

The paper introduced an extension of the Vold-Kalman Filter for better tracking of large nonstationary operating regimes. This extension is achieved by dynamically adapting the filter's bandwidth to accommodate fluctuations in speed. In the preliminary analysis, the frequency response function is also examined to provide insights into the filter's behavior. Numerical simulations are conducted to evaluate and compare the performance of conventional techniques against the proposed methodology. Additionally, the dependency on speed fluctuations is tested in a real-world application, specifically for enhanced bearing diagnostics. The adaptability to speed fluctuations ensures consistent and accurate performance across varying operational conditions, enhancing the effectiveness of machinery health monitoring. Looking ahead, future research could explore extending the proposed methodology to a higher filter order and automating the hyperparameter selection.

Acknowledgment

Fadi Karkafi gratefully acknowledges the European Commission for its support of the Marie Skłodowska Curie program through the ETN MOIRA project (GA 955681).

References

Abboud, D., Antoni, J., Sieg-Zieba, S., & Eltabach, M. (2016). Deterministic-random separation in nonstationary regime. *Journal of Sound and Vibration*, *362*, 305–326.

Abboud, D., Assoumane, A., Marnissi, Y., & El Badaoui, M. (2019). Synchronous fitting for deterministic signal extraction in non-stationary regimes: Application to helicopter vibrations.

Abboud, D., Marnissi, Y., Assoumane, A., Hawwari, Y., & Elbadaoui, M. (2022). Synchronous analysis of cyclo-non-stationary signals: A comprehensive study with aeronautic applications. *Mechanical Systems and Signal Processing*, *168*, 108600. doi: 10.1016/j.ymssp.2021.108600

Antoni, J. (2009). Cyclostationarity by examples. *Mech. Syst. Signal Process.*, *23*(4), 987–1036.

Antoni, J., & Randall, R. B. (2002). Differential diagnosis of gear and bearing faults. *J Vib Acoust*, *124*(2), 165–171.

Antoni, J., & Randall, R. B. (2007). Fast computation of the kurtogram for the detection of transient faults. *Mechanical Systems and Signal Processing*, *20*(1), 108–124.

Bonnardot, F., El Badaoui, M., Randall, R. B., Daniere, J., & Guillet, F. (2005). Use of the acceleration signal of a gearbox in order to perform angular resampling (with limited speed fluctuation). *Mech. Syst. Signal Process.*, *19*(4), 766–785.

Borghesani, P., Pennacchi, P., Randall, R. B., & Ricci, R. (2012). Order tracking for discrete-random separation in variable speed conditions. *Mech. Syst. Signal Process.*, *30*, 1–22.

Braun, S. (1975). The extraction of periodic waveforms by time domain averaging. *Acta Acustica United with Acustica*, *32*(2), 69–77.

Braun, S. (1986). Mechanical signature analysis: theory and applications.

Daher, Z., Sekko, E., Antoni, J., Capdessus, C., & Allam, L. (2010). Estimation of the synchronous average under varying rotating speed condition for vibration monitoring. *Journal of Sound and Vibration*.

Dion, J.-L., Stephan, C., Chevallier, G., & Festjens, H. (2013). Tracking and removing modulated sinusoidal components: A solution based on the kurtosis and the extended kalman filter. *Mechanical Systems and Signal Processing*, *38*(2), 428–439. doi: 10.1016/j.ymssp.2013.04.001

Feng, K., Ji, J., Wang, K., Wei, D., Zhou, C., & Ni, Q. (2022). A novel order spectrum-based vold-kalman filter bandwidth selection scheme for fault diagnosis of gearbox in offshore wind turbines. *Ocean Engineering*, *266*(Part 3), 112920. doi: 10.1016/j.oceaneng.2022.112920

McFadden, P. D. (1987). A revised model for the extraction of periodic waveforms by time domain averaging. *Mechanical Systems and Signal Processing*, *1*(1), 83–95.

McFadden, P. D. (1989). Interpolation techniques for time domain averaging of gear vibration. *Mech. Syst. Signal Process.*, *3*(1), 87–97.

Pai, P. F., & Palazotto, A. N. (2009, May 4-7). Online frequency and amplitude tracking of nonlinear non-stationary structural vibration. In *50th aiaa/asme/asce/ahs/asc structures, structural dynamics, and materials conference.* Palm Springs, California.

Pan, M., Chu, W., & Le, D.-D. (2016). Adaptive angular-velocity vold–kalman filter order tracking–theoretical basis, numerical implementation and parameter investigation. *Mech. Syst. Signal Process.*, *81*, 148–161.

Pan, M.-C., & Wu, C.-X. (2007a). Adaptive angular-displacement vold-kalman order tracking. In *2007 ieee international conference on acoustics, speech and signal processing - icassp '07* (pp. III-1293–III-1296). doi: 10.1109/ICASSP.2007.367081

Pan, M.-C., & Wu, C.-X. (2007b). Adaptive vold–kalman filtering order tracking. *Mech. Syst. Signal Process.*, *21*(8), 2957–2969.

Randall, R. B., & Antoni, J. (2011). Rolling element bearing diagnostics—a tutorial. *Mech. Syst. Signal Process.*, *25*(2), 485–520.

Randall, R. B., Sawalhi, N., & Coats, M. (2011). A comparison of methods for separation of deterministic and random signals. *Int. J. Cond. Monit.*, *1*(1), 11–19.

Savitzky, A., & Golay, M. (1964). Smoothing and differentiation of data by simplified least squares procedures. *Analytical Chemistry*, *36*(8), 1627–1639. doi: 10.1021/ac60214a047

Vold, H., Mains, M., & Blough, J. (1997). Theoretical foundations for high performance order tracking with the vold-kalman tracking filter. In *Sae technical paper.* Retrieved from `https://doi.org/10.4271/972007` doi: 10.4271/972007

Yazdanianasr, M., Verwimp, T., Karkafi, F., Mauricio, A., & Gryllias, K. (2024). *Acoustics dataset of damaged rolling element bearings captured using a smart phone at the ku leuven lmsd diagnostics test rig.* `https://doi.org/10.48804/XBN2QC`. KU Leuven RDR.